3216 *Inorg. Chem.* **2010**, *49*, 3216–3223
DOI: 10.1021/ic902072v

Inorganic Chemistry
Article

Correlation between the Structural Distortions and Thermoelectric Characteristics in $La_{1-x}A_xCoO_3$ (A = Ca and Sr)

Yang Wang,[†,‡] Yu Sui,[*,‡,§] Peng Ren,[†] Lan Wang,[†] Xianjie Wang,[‡] Wenhui Su,[‡] and Hong Jin Fan[*,†]

[†]*Division of Physics and Applied Physics, School of Physical and Mathematical Sciences, Nanyang Technological University, 21 Nanyang Link, 637371 Singapore, Singapore,* [‡]*Center for Condensed Matter Science and Technology (CCMST), Department of Physics, Harbin Institute of Technology, Harbin 150001, People's Republic of China, and* [§]*International Center for Materials Physics, Academia Sinica, Shenyang 110015, People's Republic of China*

Received October 20, 2009

Detailed structures and thermoelectric (TE) properties are investigated for the perovskite $La_{1-x}Ca_xCoO_3$ and $La_{1-x}Sr_xCoO_3$ with $0 \leq x \leq 0.3$. The monoclinic crystal structures for all samples are refined from powder X-ray diffraction, which reveals that the $La_{1-x}Sr_xCoO_3$ series has smaller global distortions but larger local distortions. The different structural distortions strongly influence the transport and TE properties in terms of resistivity, thermopower, thermal conductivity, bandwidth, and effective mass as well as electronic correlation. These results unambiguously demonstrate a close correlation between the structural distortions and TE characteristics in this family. Furthermore, a new approach is suggested to improve the TE performance by controlling the structure factors in such strongly correlated oxide systems. The effects of the spin-state transition of Co ions on the TE properties are also discussed.

Introduction

Recently, as one type of energy conversion technology, thermoelectric (TE) energy conversion has received increasing attention. TE materials are solid-state energy converters of which the combination of thermal and electrical properties allows them to directly convert waste heat into electricity or electrical power into cooling and heating.[1,2] The advantages of TE devices include solid-state operation, vast scalability, zero emissions, no maintenance, and long lifetime. Usually, the efficiency of TE materials is described by a dimensionless figure of merit $ZT = S^2T/\rho\kappa$, where S, ρ, and κ are thermopower, resistivity, and thermal conductivity, respectively. For practical applications, $ZT > 1$ is required. Among TE materials, metal oxides are more suitable for high-temperature TE applications than metal alloys because of the structural and chemical stabilities, oxidation resistance, and low cost of metal oxides. Although the performances of earlier TE oxides are very far from application criterion, the recent discovery of a large TE response in some 3d transition-metal oxides (e.g., cobaltites, titanates, and manganites) has aroused renewed interest.[3−8]

Among these metal oxides, perovskite-type cobaltites $R_{1-x}A_xCoO_3$ (R denotes a rare earth, and A denotes an alkaline earth) exhibit rich physical properties, such as complex spin-state transitions and spin glass behavior.[9,10] For example, for the $La_{1-x}Ca/Sr_xCoO_3$ system, the parent $LaCoO_3$ has a nonmagnetic insulating-like ground state; with increasing temperature, a paramagnetic insulating state gradually develops above ∼100 K and an insulator−metal transition occurs around 500 K.[10] The spin-state transition of Co^{3+} in $LaCoO_3$ at around 100 K remains controversial, but the low-spin (LS; t_{2g}^6) to intermediate-spin (IS; $t_{2g}^5e_g^1$) scenario is a consensus and is consistent with many experimental results.[11] By divalent Ca^{2+} or Sr^{2+} doping, the nonmagnetic ground state is strongly suppressed, and the LS−IS transition is shifted to lower temperatures, which suggests that doping stabilizes the IS state.[12] Usually, light

*To whom correspondence should be addressed. E-mail: fanhj@ntu.edu.sg (H.J.F.), suiyu@hit.edu.cn (Y.S.).

(1) Bell, L. E. *Science* **2008**, *321*, 1457.
(2) Snyder, G. J.; Toberer, E. S. *Nat. Mater.* **2008**, *7*, 105.
(3) Terasaki, I.; Sasago, Y.; Uchinokura, K. *Phys. Rev. B* **1997**, *56*, R12685.
(4) Ohta, H.; Sugiura, K.; Koumoto, K. *Inorg. Chem.* **2008**, *47*, 8429.
(5) Androulakis, J.; Migiakis, P.; Giapintzakis, J. *Appl. Phys. Lett.* **2004**, *84*, 1099.
(6) Masset, A. C.; Michel, C.; Maignan, A.; Hervieu, M.; Toulemonde, O.; Studer, F.; Raveau, B.; Hejtmanek, J. *Phys. Rev. B* **2000**, *62*, 166.
(7) Flahaut, D.; Mihara, T.; Funahashi, R.; Nabeshima, N.; Lee, K.; Ohta, H.; Koumoto, K. *J. Appl. Phys.* **2006**, *100*, 084911.
(8) Bocher, L.; Aguirre, M. H.; Logvinovich, D.; Shkabko, A.; Robert, R.; Trottmann, M.; Weidenkaff, A. *Inorg. Chem.* **2008**, *47*, 8077.
(9) Takami, T.; Zhou, J. S.; Goodenough, J. B.; Ikuta, H. *Phys. Rev. B* **2007**, *76*, 144116.
(10) Kriener, M.; Zobel, C.; Reichl, A.; Baier, J.; Cwik, M.; Berggold, K.; Kierspel, H.; Zabara, O.; Freimuth, A.; Lorenz, T. *Phys. Rev. B* **2004**, *69*, 094417.
(11) Kobayashi, Y.; Fujiwara, N.; Murata, S.; Asai, K.; Yasuoka, H. *Phys. Rev. B* **2000**, *62*, 410.
(12) Tokura, Y.; Okimoto, Y.; Yamaguchi, S.; Taniguchi, H.; Kimura, T.; Takagi, H. *Phys. Rev. B* **1998**, *58*, R1699.

 Published on Web 03/05/2010

doping can lead to spin glass behavior, whereas heavier doping causes ferromagnetic ordering.[13,14] Particularly, the $La_{1-x}Ca/Sr_xCoO_3$ family shows good TE characteristics for reasons that are not fully understood; the spin degeneracy of Co ions may be a possible source.[15] It has been reported that the ZT value of $La_{1-x}Sr_xCoO_3$ ceramics can reach 0.18 at 300 K.[5] Nevertheless, because of the relatively high κ in single crystals, ZT of $La_{1-x}Sr_xCoO_3$ single crystals is much smaller than that of ceramic samples.[16] To optimize the TE properties of this cobalt oxide family, several investigations have been conducted.[17−23] However, most of this research concerns only the TE results but pays little attention to the factors determining the TE response in this family. Systematic and detailed studies are still scanty.

In addition, the crystal structure of the $La_{1-x}A_xCoO_3$ system also remains controversial. Although the crystal structure of $LaCoO_3$ has been interpreted to have rhombohedral $R\bar{3}c$ symmetry for a long time,[24,25] this space group is incompatible with cooperative Jahn−Teller (JT) distortion because Co^{3+} (IS) is strongly JT-active. Recent high-resolution X-ray studies revealed that $LaCoO_3$ has monoclinic distortion (space group $I2/a$) above 90 K,[9,26] compatible with JT distortion. Considering the strong coupling between the structure and physical properties, in this study, we focus on the effects of structural distortions on the TE characteristics of Ca- and Sr-doped $LaCoO_3$ and discuss the different TE properties in these two systems. By step-scanned X-ray diffraction (XRD) data, good refinement results based on space group $I2/a$ were obtained. Then we found that $La_{1-x}Ca_xCoO_3$ and $La_{1-x}Sr_xCoO_3$ do not have identical global and local distortions, and the different structural distortions induced by Ca and Sr doping are responsible for the different TE responses.

Experimental Section

Polycrystalline samples of $La_{1-x}Ca_xCoO_3$ and $La_{1-x}Sr_xCoO_3$ with $0 \le x \le 0.3$ were prepared by a standard solid-state reaction. Reagent-grade La_2O_3, Co_3O_4, $CaCO_3$, and $SrCO_3$ powders were mixed in stoichiometric quantities and calcined in air at 1273 K for 24 h. Then the mixture was ground, pressed into disk-shaped pellets, and sintered in air at 1373 K for 24 h. Finally, in order to get compact ceramic samples, the products were repeatedly ground, cold-pressed into pellets under a high pressure of 3 GPa with a special steel die, and then sintered in air at 1473 K for 24 h. The pellets were slowly cooled down to room temperature in a furnace.

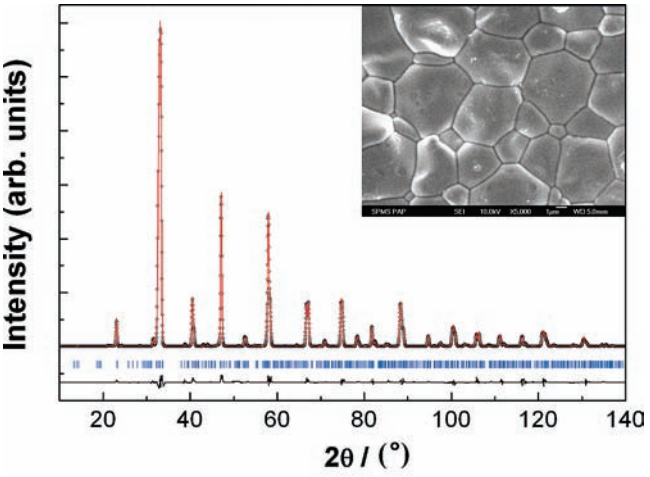

Figure 1. XRD patterns and Rietveld refinement results for $La_{0.7}Ca_{0.3}CoO_3$ at room temperature. The experimental data are shown as dots; the global fitting profile and the difference curve are shown as solid lines; the calculated reflection positions are indicated by stick marks. The inset shows the SEM micrograph of $La_{0.7}Ca_{0.3}CoO_3$.

Powder XRD data at room temperature were collected using an XRD diffractometer (D8 Advanced) with Cu Kα (λ = 0.154 06 nm) radiation. The data were collected from 10° up to 140° in 2θ with 0.02° steps and a counting time of 30 s per step. The O content in the samples was determined by iodometic titration. The results show that the oxygen stoichiometry for all of the samples is equal to 3.00, except for $x = 0.3$ samples, whose oxygen stoichiometry is ~2.98−2.99. The microstructure was observed with a JEOL JSM-6700F scanning electron microscope. Temperature dependences of resistivity, thermopower, thermal conductivity, and the Hall coefficient were all measured by using the commercial Quantum Design physical property measurement system. Disk-shaped samples were cut into bars in dimensions of 10 mm × 1 mm × 1 mm. Resistivity and thermopower measurements were performed by a standard four-probe method, whereas the Hall coefficient was measured using a five-probe method, with copper wire as leads. Thermal conductivity and specific heat were measured using a steady-state technique in a closed-cycle refrigerator pumped down to 10^{-5} Torr.

Results and Discussion

Doping-Induced Structural Distortions. The XRD pattern and scanning electron microscopy (SEM) micrograph for $La_{0.7}Ca_{0.3}CoO_3$ are shown in Figure 1. Other samples have similar XRD patterns and microstructure. The SEM micrographs indicate that these ceramics fabricated by a cold high-pressure method are quite dense, without obvious pores. The typical grain size is ~3−5 μm. The XRD data confirm the single-phase nature of the synthesized compounds. The structural parameters, as summarized in Table 1, were determined by the Rietveld refinement method, using the profile analysis program *Fullprof*. Herein the reliability factors R_{wp}, R_B, and R_F mean weighed profile, Bragg factor, and crystallographic factor, respectively. The Rietveld refinement of all of the samples was carried out by considering a monoclinic structure described by space group $I2/a$. As mentioned already, most neutron diffraction or XRD experiments of $LaCoO_3$ have been interpreted in rhombohedral space

(13) Sathe, V. G.; Pimpale, A. V.; Siruguri, V.; Paranjpe, S. K. *J. Phys.: Condens. Matter* **1996**, *8*, 3889.
(14) Wu, J.; Leighton, C. *Phys. Rev. B* **2003**, *67*, 174408.
(15) Koshibae, W.; Tsutsui, K.; Maekawa, S. *Phys. Rev. B* **2000**, *62*, 6869.
(16) Berggold, K.; Kriener, M.; Zobel, C.; Reichl, A.; Reuther, M.; Müller, R.; Freimuth, A.; Lorenz, T. *Phys. Rev. B* **2005**, *72*, 155116.
(17) Robert, R.; Bocher, L.; Trottmann, M.; Reller, A.; Weidenkaff, A. *J. Solid State Chem.* **2006**, *179*, 3839.
(18) He, T.; Chen, T. G.; Calvarese, T. G.; Subramanian, M. A. *Solid State Sci.* **2006**, *8*, 467.
(19) Hébert, S.; Flahaut, D.; Martin, C.; Lemonnier, S.; Noudem, J.; Goupil, C.; Maignan, A.; Hejtmanek, J. *Prog. Solid State Chem.* **2007**, *35*, 457.
(20) Zhou, A. J.; Zhu, T. J.; Zhao, X. B. *Mater. Sci. Eng., B* **2006**, *128*, 174.
(21) Zhang, X.; Li, X. M.; Chen, T. L.; Chen, L. D. *J. Cryst. Growth* **2006**, *286*, 1.
(22) Liu, Y.; Qin, X. Y.; Xin, H. X.; Zhang, J.; Li, H. J.; Wang, Y. F. *J. Appl. Phys.* **2007**, *101*, 083709.
(23) Iwasaki, K.; Ito, T.; Nagasaki, T.; Arita, Y.; Yoshino, M.; Matsui, T. *J. Solid State Chem.* **2008**, *181*, 3145.
(24) Thornton, G.; Tofield, B. C.; Hewat, A. W. *J. Solid State Chem.* **1986**, *61*, 301.
(25) Radaelli, P. G.; Cheong, S. W. *Phys. Rev. B* **2002**, *66*, 094408.
(26) Maris, G.; Ren, Y.; Volotchaev, V.; Zobel, C.; Lorenz, T.; Palstra, T. T. M. *Phys. Rev. B* **2003**, *67*, 224423.

Table 1. Refined Cell Parameters, Atomic Positions, Isotropic Thermal Factor B_{iso}, Fitting Factors (R_{wp}, R_B, and R_F), A-Site Average Ionic Radii $\langle r_A \rangle$, A-Site Cation Size Variance σ^2, and Tolerance Factor t for All of the Samples

		$La_{1-x}Ca_xCoO_3$				$La_{1-x}Sr_xCoO_3$			
	$LaCoO_3$	$x = 0.05$	$x = 0.1$	$x = 0.2$	$x = 0.3$	$x = 0.05$	$x = 0.1$	$x = 0.2$	$x = 0.3$
a (Å)	5.3682(3)	5.3671(4)	5.3633(3)	5.3595(5)	5.3522(3)	5.3698(4)	5.3716(4)	5.3881(3)	5.4018(5)
b (Å)	5.4326(4)	5.4321(4)	5.4315(5)	5.4304(3)	5.4289(2)	5.4335(3)	5.4343(4)	5.4365(4)	5.4396(4)
c (Å)	7.6386(5)	7.6376(3)	7.6357(4)	7.6329(5)	7.6298(4)	7.6421(4)	7.6469(5)	7.6543(5)	7.6604(5)
β (deg)	90.9818(7)	90.9537(8)	90.9263(7)	90.8735(9)	90.8116(8)	90.8856(7)	90.8124(8)	90.6715(8)	90.4643(9)
$y_{La/Ca/Sr}$	0.24911(14)	0.24934(10)	0.24951(15)	0.24976(12)	0.24985(13)	0.24942(13)	0.24975(17)	0.24993(12)	0.25046(16)
B_{iso}(La/Ca/Sr) (Å^2)	0.18(2)	0.18(3)	0.19(3)	0.18(2)	0.17(3)	0.17(2)	0.17(2)	0.16(2)	0.16(3)
B_{iso}(Co) (Å^2)	0.39(3)	0.40(3)	0.41(3)	0.40(4)	0.42(5)	0.41(4)	0.39(4)	0.40(4)	0.42(5)
$y_{O(1)}$	−0.29973(16)	−0.29635(15)	−0.29372(18)	−0.28841(23)	−0.28882(17)	−0.29134(17)	−0.28879(21)	−0.28365(18)	−0.28517(20)
B_{iso}[O(1)] (Å^2)	0.52(3)	0.54(4)	0.53(3)	0.54(3)	0.52(4)	0.55(3)	0.55(4)	0.56(4)	0.58(4)
$x_{O(2)}$	0.02129(13)	0.02115(12)	0.02101(15)	0.02058(13)	0.01934(18)	0.02104(14)	0.02087(12)	0.02036(15)	0.0187(16)
$y_{O(2)}$	0.03604(14)	0.03634(15)	0.03628(12)	0.03673(11)	0.03725(15)	0.03659(13)	0.03713(14)	0.03766(12)	0.03772(13)
$z_{O(2)}$	0.22865(24)	0.22891(19)	0.22902(21)	0.22905(17)	0.22897(22)	0.22885(23)	0.22893(18)	0.23011(17)	0.23163(22)
B_{iso}[O(2)] (Å^2)	0.65(3)	0.63(4)	0.62(4)	0.63(3)	0.62(4)	0.64(3)	0.64(4)	0.63(4)	0.63(3)
R_{wp} (%)	6.22	6.12	6.03	5.87	5.96	5.95	6.13	5.83	5.92
R_B (%)	3.36	3.34	3.78	3.55	3.47	3.44	3.61	3.82	3.71
R_F (%)	2.58	2.61	2.72	2.57	2.62	2.69	2.58	2.66	2.59
$\langle r_A \rangle$ (Å)	1.2160	1.2142	1.2124	1.2088	1.2052	1.2207	1.2254	1.2348	1.2442
σ^2 (Å^2)	0	0.00006	0.00012	0.00021	0.00027	0.00042	0.00079	0.00141	0.00186
t	0.92029	0.92136	0.92270	0.92513	0.92757	0.92365	0.92729	0.93435	0.94146

group $R\bar{3}c$.[24,25] However, Maris et al. recently found the monoclinic distortion for $LaCoO_3$ by performing a high-angular-resolution scan using synchrotron radiation, and they analyzed their XRD data based on $I2/a$ symmetry, which was well consistent with the observed JT distortion.[26] Also, Takami et al. refined their XRD spectra of $La_{1-x}Sr_xCoO_3$ ($0 \le x \le 0.3$) in both space groups $R\bar{3}c$ and $I2/a$ and found that the R factors of the fits were smaller when the space group $I2/a$ was assumed.[9] Hence, we also refined our XRD data on the basis of $I2/a$ monoclinic perovskite symmetry, with $a \sim b \sim 2^{1/2}a_p$ and $c \sim 2a_p$ (where a_p is the lattice parameter of an ideal cubic perovskite structure). As can be seen in Figure 1, all of the reflections can be indexed by a monoclinic perovskite structure and good agreement is obtained between the observed and calculated XRD patterns. The refined quality factors (R_{wp}, R_B, and R_F) of all samples are small, ensuring the high reliability of the refinement.

From Table 1, one can find that the lattice parameters a, b, and c decrease slightly with an increase in the Ca content, whereas Sr doping causes an increase in all of the a-, b-, and c-axis lengths. This should be attributed to the variation of the A-site radius because the ionic radius of La^{3+} (1.216 Å) is much smaller than that of Sr^{2+} (1.31 Å) but only slightly larger than that of Ca^{2+} (1.18 Å). (Here we use the nine-coordinated A-site ionic radii because the coordination number in orthorhombic or monoclinic distorted perovskites is usually nine.) It should be noted that, while Sr doping brings Co^{4+} ions into the Co^{3+} matrix, the ionic radii of Co^{4+} (0.53 Å) and Co^{3+} (0.545 Å) are very close. Therefore, the increase in the lattice parameters in $La_{1-x}Sr_xCoO_3$ is mainly due to the size difference between Sr^{2+} and La^{3+}. For these two dopings, the monoclinic angle β systematically decreases with an increase in the Ca/Sr content, implying that a higher symmetry (orthorhombic or cubic) is approached. The tolerance factor t, defined as $t = (r_A + r_O)/2^{1/2}(r_B + r_O)$,[27] was also calculated for all of the samples. t gradually increases with doping, which also suggests a decrease of global distortions. Furthermore, Sr-doped samples show lower β and larger t, indicating that they have lower global distortions than Ca-doped samples, although they have larger size mismatching σ^2 (defined by $\sigma^2 = \sum y_i r_i^2 - \langle r_A \rangle^2$, where r_i is the ionic radius, y_i is the fractional occupancy of the ith atoms of the A site, and $\langle r_A \rangle$ is the average A-site radius).

Figure 2 shows variations of the bond length d_{Co-O} and the bond angle $\theta_{Co-O-Co}$ as a function of the doping level x determined by structure analysis. In $I2/a$ symmetry, there are two different Co−O−Co bond angles, both of which increase as the Ca/Sr content increases. The increasing $\theta_{Co-O-Co}$ consists of alterations of β and t, meaning reductions of the global structure distortion. Also, $\theta_{Co-O-Co}$ of Sr-doped samples is closer to an ideal 180° than that of Ca-doped samples, corresponding to the lighter global distortion in the $La_{1-x}Sr_xCoO_3$ series. In $R\bar{3}c$ symmetry, all of the Co−O bond lengths are identical, so JT distortion cannot exist. However, unlike space group $R\bar{3}c$, there are three unequal Co−O bond lengths in space group $I2/a$, one Co−O(1) and two Co−O(2). As can been seen from Figure 2a, all samples show a clear difference in the bond lengths, indicating that these samples are JT-distorted. With Ca or Sr doping, Co−O(1) exhibits only a quite weak x dependence, while one Co−O(2) increases but the other Co−O(2) decreases as x increases. This behavior suggests that the local CoO_6 octahedral-site distortion (or JT distortion) is enhanced by doping. In addition, Sr doping induces a more notable separation between the two Co−O(2) bonds, which indicates that the $La_{1-x}Sr_xCoO_3$ series has more evident local CoO_6 distortion than $La_{1-x}Ca_xCoO_3$.

In order to probe the local distortion in this system, variations of the JT distortion (calculated by dividing the difference between the two Co−O(2) bond lengths by their average) along with CoO_6 octahedral distortion are plotted in Figure 3. As we know, CoO_6 octahedra in $LaCoO_3$ with the perovskite structure are not rigid. The cooperative tilts and rotations of the CoO_6 octahedra are

(27) Goldschmidt, V. M. *Naturwissenschaften* **1926**, *14*, 477.

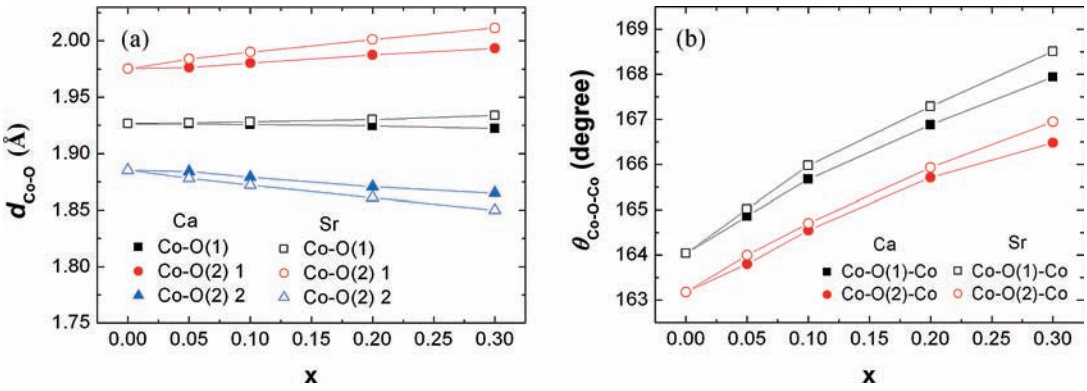

Figure 2. (a) Bond length d_{Co-O} and (b) bond angle $\theta_{Co-O-Co}$ as a function of doping level x for $La_{1-x}Ca_xCoO_3$ and $La_{1-x}Sr_xCoO_3$.

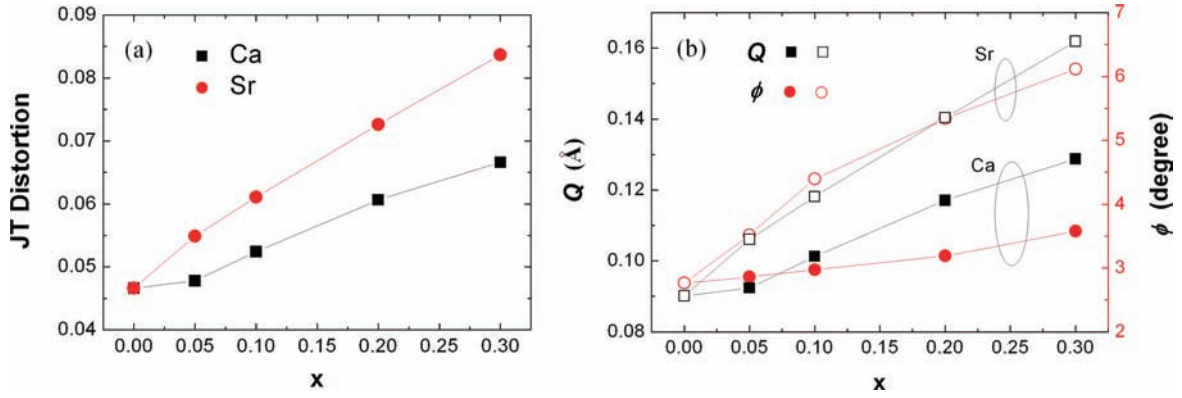

Figure 3. x dependence of (a) JT distortion and (b) Q and ϕ for $La_{1-x}Ca_xCoO_3$ and $La_{1-x}Sr_xCoO_3$.

around all three axes, which change the cubic lattice parameters from $a_p \times a_p \times a_p$ to $a \sim 2^{1/2}a_p$, $b \sim 2^{1/2}a_p$, and $c \sim 2a_p$ and cause the bending of Co−O−Co bond angles and the splitting of Co−O bond lengths. The bond-length splitting can be described by two degenerate vibrational modes, Q_2 and Q_3, determined by $Q_2 = d_{Co-O(2)1} - d_{Co-O(2)2}$ and $Q_3 = (2d_{Co-O(1)} - d_{Co-O(2)1} - d_{Co-O(2)2})/3^{1/2}$. In addition to JT distortion, two distortion parameters $Q = (Q_2^2 + Q_3^2)^{1/2}$ and $\phi = \tan^{-1}(Q_3/Q_2)$ can directly reflect the local CoO_6 distortion in this system. Figure 3 clearly indicates that the local distortions (including the degree of JT distortion, Q, and ϕ) increase with doping, although the global distortion decreases as mentioned above. The enhanced local distortion can be well correlated with the behavior of the spin-state transition with Ca/Sr doping.[9] The temperature of the spin-state transition, which is ~100 K for undoped $LaCoO_3$, decreases with the substitution of Ca^{2+} or Sr^{2+} for La^{3+}. Consequently, doping stabilizes the IS state, so the population of the JT-active IS state increases, resulting in an increase in the CoO_6 local distortion. It should be noted that these enhanced local distortions cannot be revealed by the usual structural parameters (monoclinic angle, bond angle, and tolerance factor). Additionally, compared with $La_{1-x}Ca_xCoO_3$, the $La_{1-x}Sr_xCoO_3$ series has smaller global distortion but larger local distortion because it shows higher degree of JT distortion, Q, and ϕ. In the following, we will see that these doping-induced structural distortions strongly influence the TE characteristics in this system.

Effects of Doping on Electric Transport. All of the $La_{1-x}Ca_xCoO_3$ samples exhibit semiconducting-like behavior (i.e., $d\rho/dT < 0$), and ρ decreases observably with increasing x (see Figure 4). The reduction of ρ with doping can be attributed to an increase in the carrier concentration n as well as the mobility μ. By Hall coefficient measurements, the evaluated n and μ monotonically increase with the Ca/Sr content (see Table 2). In this family, the substitution of Ca^{2+} or Sr^{2+} for La^{3+} will yield large numbers of hole carriers based on the valence equilibrium, which can facilitate the carrier transport and thus lower ρ. Moreover, the increase in n is considerable for lightly doped samples, whereas it becomes gentle for heavily doped samples, suggesting that the doped carrier is nearly saturated. In contrast, the enhancement of μ becomes noticeable with gradual doping, which implies that μ plays a more important role in ρ for heavily doped samples. $La_{1-x}Sr_xCoO_3$ has similar $\rho-T$ curves except that $La_{0.7}Sr_{0.3}CoO_3$ shows a metallic-like behavior (i.e., $d\rho/dT > 0$; see the inset of Figure 4b). Overall, the temperature and doping level dependences of ρ agree well with previous studies.[10,23,28] In addition, herein the ρ data are very close to those of reported single-crystal samples (usually, the metallic-like transport of $La_{0.7}Sr_{0.3}CoO_3$ can only be observed in single-crystal samples).[10,29] Hence, it implies that in our highly compact ceramics, which were fabricated by the cold high-pressure method, the grain

(28) Onose, Y.; Tokura, Y. *Phys. Rev. B* **2006**, *73*, 174421.
(29) Kobayashi, Y.; Murata, S.; Asai, K.; Tranquada, J. M.; Shirane, G.; Kohn, K. *J. Phys. Soc. Jpn.* **1999**, *68*, 1011.

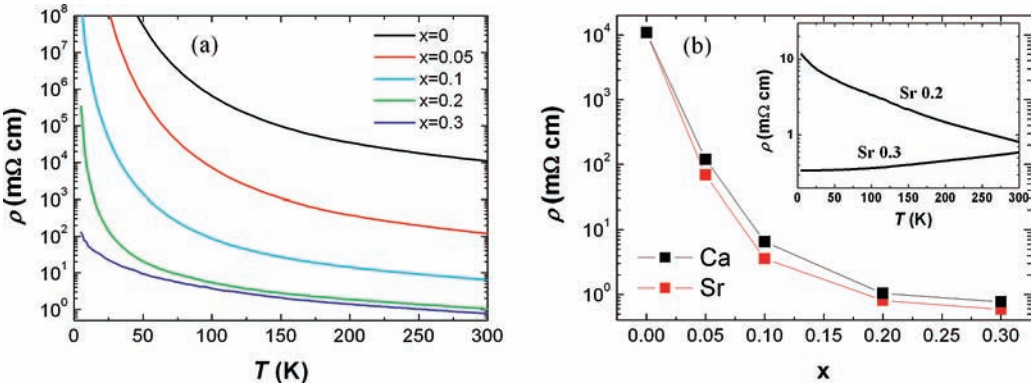

Figure 4. (a) Temperature dependence of resistivity ρ for $La_{1-x}Ca_xCoO_3$. (b) Room-temperature resistivity as a function of x for $La_{1-x}Ca_xCoO_3$ and $La_{1-x}Sr_xCoO_3$. The inset of part b presents $\rho-T$ curves of $La_{0.8}Sr_{0.2}CoO_3$ and $La_{0.7}Sr_{0.3}CoO_3$.

Table 2. Room-Temperature Carrier Concentration n, Carrier Mobility μ, Effective Mass m^*, Relaxation Time τ, and Bandwidth W as Well as ρ, S, κ, and ZT at 300 K

	x	n ($\times 10^{21}$ cm^{-3})	μ (cm^2 V^{-1} s^{-1})	m^* ($\times m_e$)	τ ($\times 10^{-16}$ s)	W (Å$^{-3.5}$)	$\rho_{300\ K}$ (mΩ cm)	$S_{300\ K}$ (μV K^{-1})	$\kappa_{300\ K}$ (W m^{-1} K^{-1})	$ZT_{300\ K}$
$LaCoO_3$	0	0.0126	0.026	12.66	1.87	0.009 06	10858	560.2	1.88	0.0005
$La_{1-x}Ca_xCoO_3$	0.05	3.44	0.039	9.31	2.07	0.010 62	119.2	280.3	1.98	0.0099
	0.1	5.32	0.181	6.63	6.83	0.013 78	6.51	168.8	2.32	0.0566
	0.2	6.24	0.963	3.09	16.92	0.067 79	1.04	74.2	2.91	0.0346
	0.3	6.76	1.21	1.43	9.84	0.096 35	0.77	25.5	3.29	0.0077
$La_{1-x}Sr_xCoO_3$	0.05	3.52	0.067	8.51	3.24	0.011 83	68.5	249.9	1.95	0.0141
	0.1	5.61	0.313	5.27	9.38	0.019 48	3.58	159.7	2.20	0.0972
	0.2	6.47	1.20	2.78	18.97	0.076 99	0.81	62.4	2.75	0.0524
	0.3	7.02	1.51	1.32	11.34	0.099 44	0.59	21.1	3.16	0.0072

boundaries have a negligible influence on the carrier conduction.

The differences in room-temperature resistivity between $La_{1-x}Ca_xCoO_3$ and $La_{1-x}Sr_xCoO_3$ are shown in Figure 4b. For the same doping level, $La_{1-x}Sr_xCoO_3$ exhibits lower ρ (this ρ distinction actually exists not only at room temperature but also in the whole measured temperature range). From the Hall coefficient measurements, the Ca-doped series has comparable n with the Sr-doped series but has much smaller μ (especially for lightly doped samples); see Table 2. Considering the close coupling between the crystalline structure and transport properties in such a strongly correlated narrow-band system, we have to take into account the effective bandwidth determined by structure distortions. The electronic structure revealed by photoemission spectroscopy also implies that the band structure that mainly depends on the valence of Co ions has a close correlation with the transport characteristics in this system.[30−32] On the basis of the refinement results, the bandwidth W of this family can be estimated by

$$W \propto \frac{\cos[(\pi - \overline{\theta}_{Co-O-Co})/2]}{\overline{d}_{Co-O}^{7/2}} \quad (1)$$

where $\overline{d}_{Co-O}$ and $\bar{\theta}_{Co-O-Co}$ are the average Co−O bond length and Co−O−Co bond angle, respectively.[33] The calculated W is listed in Table 2. W monotonously increases with x, corresponding to decreasing ρ. Because for the Ca-doped series the deviation from cubic symmetry is more pronounced compared with that of the Sr-doped samples, the former has a stronger deviation of the Co−O−Co angle from 180°, and correspondingly the bandwidth (i.e., hopping integral) is smaller than that of $La_{1-x}Sr_xCoO_3$. As a consequence, the $La_{1-x}Ca_xCoO_3$ series shows higher ρ in the same doping level and remains semiconducting-like even for $x = 0.3$. For $La_{0.7}Sr_{0.3}CoO_3$, when the bandwidth increases to approach the narrow-band limit of itinerant electrons, the compound shows a metallic $\rho-T$ curve; namely, a doping-induced metal−semiconductor transition occurs. In summary, this result suggests that structural variation by doping has a strong effect on the electrical transport; higher symmetry and lower global distortion (i.e., $La_{1-x}Sr_xCoO_3$ system) are advantageous to the enhancement of electric conduction.

Figure 5a presents thermopower S versus temperature of $La_{1-x}Ca_xCoO_3$. Similar temperature and x dependences were observed in $La_{1-x}Sr_xCoO_3$. The signs of S for all of the samples are positive, indicating the nature of the hole carrier in this system, as is consistent with the Hall coefficient measurements. It has been reported that undoped $LaCoO_3$ can show both positive and negative S[16,34] because S of pure $LaCoO_3$ is extremely sensitive to the O content. The tiny deviation in the O content in $LaCoO_{3+\delta}$, which causes a small concentration 2δ of hole or electron doping, is below the accuracy of oxygen determination. Herein the positive S of our pure $LaCoO_3$ indicates that there should be a very slight excess of

(30) Pandey, S. K.; Kumar, A.; Banik, S.; Shukla, A. K.; Barman, S. R.; Pimpale, A. V. *Phys. Rev. B* **2008**, *77*, 113104.
(31) Pandey, S. K.; Kumar, A.; Patil, S.; Medicherla, V. R. R.; Singh, R. S.; Maiti, K.; Prabhakaran, D.; Boothroyd, A. T.; Pimpale, A. V. *Phys. Rev. B* **2008**, *77*, 045123.
(32) Saitoh, T.; Mizokawa, T.; Fujimori, A.; Abbate, M.; Takeda, Y.; Takano, M. *Phys. Rev. B* **1997**, *56*, 1290.
(33) Medarde, M.; Mesot, J.; Lacorre, P.; Rosenkranz, S.; Fischer, P.; Gobrecht, K. *Phys. Rev. B* **1995**, *52*, 9248.
(34) Robert, R.; Bocher, L.; Trottmann, M.; Reller, A.; Weidenkaff, A. *J. Solid State Chem.* **2006**, *179*, 3893.

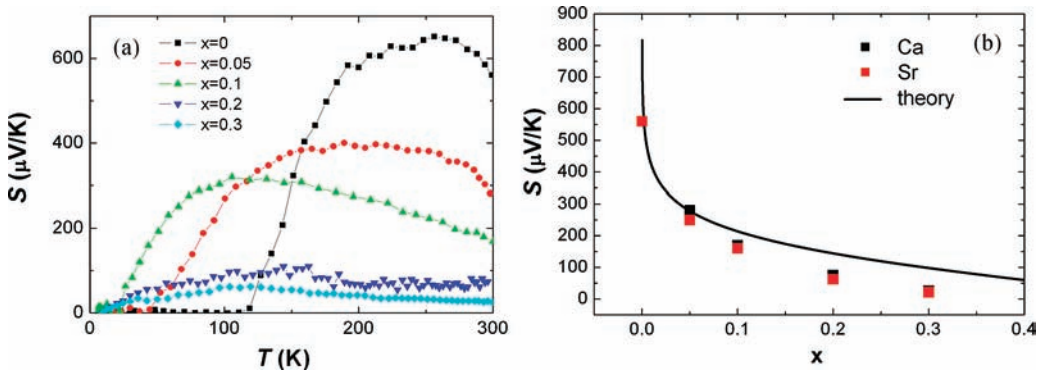

Figure 5. (a) Temperature dependence of thermopower S for $La_{1-x}Ca_xCoO_3$. (b) Room-temperature thermopower as a function of x of $La_{1-x}Ca_xCoO_3$ and $La_{1-x}Sr_xCoO_3$ together with the theory curve calculated by eq 5.

oxygen. The sharp collapse of S at around 120 K in $LaCoO_3$ may be correlated to the LS−IS transition, which alters the configuration entropy evidently. Although S of undoped $LaCoO_3$ can be either positive or negative, even a very slight doping can eliminate the influence of an excess (or vacancy) of oxygen and induce the collapse of S.[16] As mentioned above, the spin-state transition will be drastically suppressed by doping, so the S profile collapses at lower temperatures and becomes less pronounced with an increase in the doping level (see Figure 5a).

In cobaltites, the larger thermopower may originate from strong electronic correlations and large configurational entropy.[15,35−38] The strong electronic correlation causes a larger electronic effective mass m^* and a narrow band with a strong energy-dependent density of states in the vicinity of Fermi level E_F.[39] The large configurational entropy is driven by the rich spin and orbital degeneracies. In both cases, S is expected to be dependent on the carrier concentration: First, a small shift of E_F by doping will significantly alter the magnitude of S because of band narrowing due to strong correlation; second, the degeneracies will also vary with the carrier concentration because of a change in the configuration and population ratio of Co^{3+} and Co^{4+} ions. Indeed, as shown in Figure 5, S decreases monotonously with doping. The increasing carrier density can partially explain the variation of S because $S \propto \sim 1/n$ in a simple Drude picture,[40] but the change in n cannot account for the decrease of S quantitatively. In order to understand quantitatively the variation of S, we consider the effects of the electronic correlation on S and relate S to m^* by applying the Boltzmann transport model,[41] in which S is described by

$$S = \frac{k_B}{e}\left[\frac{(r+5/2)F_{r+3/2}(\zeta_F)}{(r+3/2)F_{r+1/2}(\zeta_F)} - \zeta_F\right] \quad (2)$$

where r is the scattering parameter, ζ_F is the reduced chemical potential, and $F_r(\zeta_F)$ is the Fermi integral. In this model, the relationship among n, μ, m^*, and $F_r(\zeta_F)$ is given by

$$n = 4\pi\left(\frac{2k_B m^* T}{h^2}\right)^{3/2} F_{1/2}(\zeta_F) \quad (3)$$

and

$$\mu = \frac{e\tau}{m^*} \quad (4)$$

where h is Planck's constant and τ is the relaxation time. When eqs 2−4 are combined, m^* and τ are calculated and listed in Table 2. With doping, m^* decreases monotonously, whereas τ increases first, reaches maxima at $x = 0.2$, and then decreases. The reduction of m^* is consistent with a decrease of the electron specific heat coefficient, as revealed from specific heat measurements. These results also correspond well to the above resistivity analysis. Reasons for the changes in m^* and τ are proposed as follows. The bandwidth increases with an increase in the Ca/Sr content, and as a result, m^* lessens gradually. Accordingly, Ca/Sr doping reduces the electronic correlation, which also facilitates a decrease in S. Therefore, the variation of S with doping actually originates from both an increase of the carrier concentration and a decrease of the electron correlation. Because S is proportional to the electron specific heat in strongly correlated systems,[37] a decrease in the electronic correlation (i.e., a reduction of the electron specific heat and effective mass) is also responsible for the decrease of S. The increase of τ for $x = 0-0.2$ can be also attributed to an increase of the Co−O−Co bond angle and relaxation of distortions. As for the decrease of τ for $x = 0.3$, the enhanced point defect scattering induced by the formation of oxygen defects may be a possible source, similar to the report by Iwasaki et al.[23] Finally, Figure 5b also shows that $La_{1-x}Sr_xCoO_3$ has lower S than $La_{1-x}Ca_xCoO_3$ at the same x values. It can be understood that a larger bandwidth and lighter distortion in $La_{1-x}Sr_xCoO_3$ cause smaller m^* but larger τ.

At high enough temperatures, S of doped cobaltites is expected to be determined by Heikes formula, namely

$$S = -\frac{k_B}{e}\left[\ln\left(\frac{g_3}{g_4}\right) + \ln\left(\frac{x}{1-x}\right)\right] \quad (5)$$

(35) Koshibae, W.; Maekawa, S. *Phys. Rev. Lett.* **2001**, *87*, 236603.
(36) Wang, Y. Y.; Rogado, N. S.; Cava, R. J.; Ong, N. P. *Nature* **2003**, *423*, 425.
(37) Ando, Y.; Miyamoto, N.; Segawa, K.; Kawata, T.; Terasaki, I. *Phys. Rev. B* **1999**, *60*, 10580.
(38) Limelette, P.; Hardy, V.; Auban-Senzier, P.; Jérome, D.; Flahaut, D.; Hébert, S.; Frésard, R.; Simon, Ch.; Noudem, J.; Maignan, A. *Phys. Rev. B* **2005**, *71*, 233108.
(39) Singh, D. J. *Phys. Rev. B* **2000**, *61*, 13397.
(40) Aschcroft, N. W.; Mermin, N. D. *Solid State Physics*; Holt Saunders: Philadelphia, PA, 1976.
(41) Durczewski, K.; Ausloos, M. *Phys. Rev. B* **2000**, *61*, 5303.

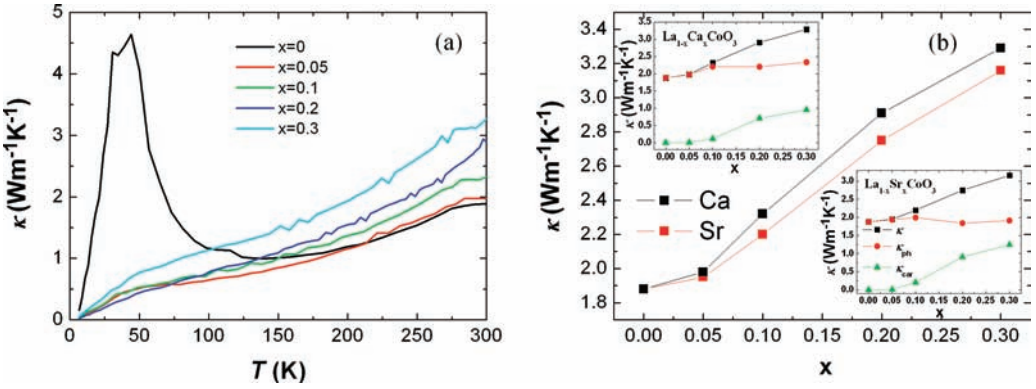

Figure 6. (a) Temperature dependence of thermal conductivity κ for $La_{1-x}Ca_xCoO_3$. (b) Thermal conductivity κ at 300 K as a function of x for $La_{1-x}Ca_xCoO_3$ and $La_{1-x}Sr_xCoO_3$. The insets of part b show x dependence of the total thermal conductivity κ, phonon thermal conductivity κ_{ph}, and carrier thermal conductivity κ_{car} at 300 K for $La_{1-x}Ca_xCoO_3$ and $La_{1-x}Sr_xCoO_3$, respectively.

in which g_3 (g_4) denotes the number of possible configurations of the Co^{3+} (Co^{4+}) ions.[15] In Figure 5b, similar to Takami et al.'s report,[42] we present the measured room-temperature values of S as a function of x along with the theory curve obtained from eq 5, in which the IS states of both Co^{3+} and Co^{4+} are adopted according to most magnetic experimental results and band calculation.[14] Although this theory assumes a high-temperature limit, Koshibae et al. pointed out that the room-temperature S of cobaltites is close to that in the high-temperature limit,[15,43] so that eq 5 can still be used approximately to describe the role of the configurational entropy in S around room temperature. On the other hand, a large discrepancy between the theory and experiment is observed at high doping levels (see Figure 5b). Because the high-temperature limit, where eq 5 is derived, corresponds to the transfer integral $I \ll k_BT$ (or bandwidth $W \ll k_BT$), this condition is not fulfilled when W (or I) is very large. Therefore, the considerable enhancement of W for heavily doped samples may violate the assumption of Koshibae's theory, which accounts for the discrepancy. Additionally, the Sr-doped series has larger W, so it exhibits a more obvious deviation.

TE Response. Values of thermal conductivity κ of the samples as a function of the temperature and doping level are presented in parts a amd b of Figure 6, respectively. Overall, κ of all of the samples shows a positive temperature dependence. The undoped $LaCoO_3$ exhibits a noticeable peak in $\kappa-T$ curves at lower temperatures, and the peak is drastically suppressed by doping. It is noted that the values and temperature dependences of κ of our samples are nearly identical with those of single-crystal samples, suggesting that grain boundaries are not important to the phonon transport.[16] In a $LaCoO_3$ insulator, the heat is usually carried by acoustic phonons. Optical phonons play a minor role because their dispersion is typically much weaker than that of the acoustic branches.[16] In addition, the carrier thermal conductivity is negligible because of the large resistivity. Hence, the low-temperature κ peak in $LaCoO_3$ results from an increase of the average free path of acoustic phonons, which is very sensitive to structural variations. In the LS state, the CoO_6 octahedra are regular because all six 3d electrons are in the t_{2g} orbitals, whereas in the IS state, the CoO_6 octahedra are expanded because of JT distortion. Therefore, when the IS → LS transition occurs, the disappearance of JT distortion can result in an increase in the phonon average free path, and thus κ of $LaCoO_3$ will show an evident revival below 100 K. As the temperature further decreases, the temperature dependence of κ follows that of specific heat, viz., $\kappa \propto C \propto T^3$ for $T \rightarrow 0$ K, so κ decreases rapidly and reaches zero finally.

With doping, κ rises gradually, and the low-temperature peak disappears. The drastic suppression of κ at low temperature arises from the enhanced local distortions for one thing, and the doping-induced disorder for another. For lightly doped samples (x = 0.05 and 0.1), the IS → LS transition occurs at lower temperatures, and the disorder (results from the differences between La^{3+} and Ca^{2+}/Sr^{2+} together with Co^{3+} and Co^{4+} and the formed magnetic polarons) is pronounced,[16,44] so the low-temperature maximum of κ is already strongly suppressed. For heavily doped samples (x = 0.2 and 0.3), the IS Co^{3+} ions become dominant in the whole temperature range, so the low-temperature peak of κ remains absent.

The increase of κ with doping is actually from the contribution by charge carriers. The doping-induced mobile charger carriers, which serve as additional scatterers for phonon, are also expected to transport heat. The insets of Figure 6b show the total thermal conductivity κ, phonon thermal conductivity κ_{ph}, and carrier thermal conductivity κ_{car} at room temperature according to $\kappa = \kappa_{ph} + \kappa_{car}$, where κ_{car} is estimated by Wiedemann–Franz's law $\kappa_{car} = L_0T/\rho$, with Lorentz constant $L_0 = \pi^2k_B^2/3e^2 = 2.45 \times 10^{-8}$ W Ω K^{-2}. One can see from these insets that $\kappa_{car} \ll \kappa$ for smaller x but κ_{car} becomes important for larger x, and the increase of the total thermal conductivity κ with doping mainly results from an increase of κ_{car}. κ_{ph} of the Sr-doped series remains unchanged but that of the Ca-doped series rises slightly, which is because $La_{1-x}Sr_xCoO_3$ has larger

(42) Takami, T.; Ikuta, H.; Mizutani, U. *Trans. Mater. Res. Soc. Jpn.* **2004**, *29*, 2777.
(43) Korotin, M. A.; Ezhov, S. Y.; Solovyev, I. V.; Anisimov, V. I. *Phys. Rev. B* **1996**, *54*, 5369.
(44) Yamaguchi, S.; Okimoto, Y.; Taniguchi, H.; Tokura, Y. *Phys. Rev. B* **1996**, *53*, R2926.

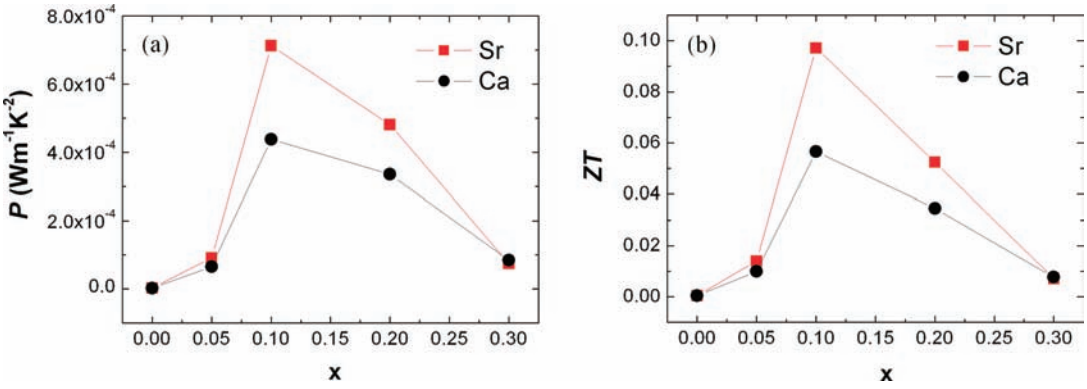

Figure 7. Room-temperature (a) power factor P and (b) figure of merit ZT as a function of x for $La_{1-x}Ca_xCoO_3$ and $La_{1-x}Sr_xCoO_3$.

local distortions that can suppress κ_{ph} more. This can also elucidate why the $La_{1-x}Sr_xCoO_3$ series has smaller global distortions and lower ρ (or, say, larger κ_{car}), but yet they show lower total thermal conductivity κ (see Figure 6b).

Using the measured ρ, S, and κ, we can calculate the TE power factor P (defined by $P = S^2/\rho$) and figure of merit ZT, as shown in Figure 7 as a function of x. Both P and ZT exhibit maxima at $x = 0.1$ in the two series. These optimal TE values ($P \sim 7.2 \times 10^{-4}$ W m^{-1} K^{-2} and $ZT \sim 0.1$ at 300 K) are among the highest observed values in metal oxides so far. Although the largest ZT is still too small for technical applications, one can expect the ZT of cobaltites to be further improved because the complex configurations and strong disorder of this system can not only enhance S but also suppress κ. Our present results also clearly reveal the close correlation between the structural distortions and the TE response in this family. Because of the distinct global/local distortions between $La_{1-x}Ca_xCoO_3$ and $La_{1-x}Sr_xCoO_3$, which biases all of the TE parameters, the $La_{1-x}Sr_xCoO_3$ series shows higher TE response than $La_{1-x}Ca_xCoO_3$, as seen in Figure 7. Furthermore, on the basis of our present results, in addition to the carrier concentration, ρ and S are also determined by the bandwidth that is controlled by global distortions, whereas κ is more dependent on local distortions. This implies that it is possible to enhance the TE response by modulating structural characteristics in this and other relevant strongly correlated oxide systems.

Conclusions

We have presented a systematic study of the structure and TE properties of the $La_{1-x}Ca_xCoO_3$ and $La_{1-x}Sr_xCoO_3$ series. All of the samples are consistently interpreted with the space group $I2/a$, which is characterized by three unequal Co−O bond lengths and is compatible with cooperative JT distortion. $La_{1-x}Sr_xCoO_3$ has smaller global distortions but larger local distortions than $La_{1-x}Ca_xCoO_3$; these structural features significantly influence the TE characteristics of the two systems. As a result, the $La_{1-x}Sr_xCoO_3$ series exhibits lower ρ, S, and κ compared with $La_{1-x}Ca_xCoO_3$. From these observations, a close correlation between the structural distortions and the TE response in this family is obtained. Owing to the different structural distortions, $La_{1-x}Sr_xCoO_3$ shows a better TE performance, and the optimal room-temperature ZT reaches 0.1 at $x = 0.1$. The correlation between structure and TEs found in this study may shed light on the ongoing search of new TE oxides among strongly correlated systems.

Acknowledgment. This work is supported by start-up funding from Nanyang Technological University to F.H.J. and the National Natural Science Foundation of China (Grants 50672019 and 10804024).